Backward-mode multiwavelength photoacoustic scanner using a planar Fabry–Perot polymer film ultrasound sensor for high-resolution three-dimensional imaging of biological tissues

Edward Zhang,* Jan Laufer, and Paul Beard

Department of Medical Physics and Bioengineering, University College London, Gower Street, London WC1E 6BT, UK

*Corresponding author: ezzhang@medphys.ucl.ac.uk

Received 21 June 2007; revised 25 September 2007; accepted 5 October 2007;
posted 10 October 2007 (Doc. ID 84398); published 25 January 2008

A multiwavelength backward-mode planar photoacoustic scanner for 3D imaging of soft tissues to depths of several millimeters with a spatial resolution in the tens to hundreds of micrometers range is described. The system comprises a tunable optical parametric oscillator laser system that provides nanosecond laser pulses between 600 and 1200 nm for generating the photoacoustic signals and an optical ultrasound mapping system based upon a Fabry–Perot polymer film sensor for detecting them. The system enables photoacoustic signals to be mapped in 2D over a 50 mm diameter aperture in steps of 10 μm with an optically defined element size of 64 μm. Two sensors were used, one with a 22 μm thick polymer film spacer and the other with a 38 μm thick spacer providing −3 dB acoustic bandwidths of 39 and 22 MHz, respectively. The measured noise equivalent pressure of the 38 μm sensor was 0.21 kPa over a 20 MHz measurement bandwidth. The instrument line-spread function (LSF) was measured as a function of position and the minimum lateral and vertical LSFs found to be 38 and 15 μm, respectively. To demonstrate the ability of the system to provide high-resolution 3D images, a range of absorbing objects were imaged. Among these was a blood vessel phantom that comprised a network of blood filled tubes of diameters ranging from 62 to 300 μm immersed in an optically scattering liquid. In addition, to demonstrate the applicability of the system to spectroscopic imaging, a phantom comprising tubes filled with dyes of different spectral characteristics was imaged at a range of wavelengths. It is considered that this type of instrument may provide a practicable alternative to piezoelectric-based photoacoustic systems for high-resolution structural and functional imaging of the skin microvasculature and other superficial structures. © 2008 Optical Society of America

OCIS codes: 110.5125, 170.3880, 170.5120, 110.7170, 170.1460.

1. Introduction

Photoacoustic imaging is a noninvasive imaging modality for visualizing the structure and function of soft tissues [1]. It relies upon irradiating the tissue surface with low energy nanosecond pulses of visible, or more deeply penetrating near-infrared (NIR) laser light. Absorption of the light by subsurface anatomical features such as blood vessels leads to impulsive heating accompanied by rapid thermoelastic expansion and the subsequent generation of broadband (tens of megahertz) ultrasonic pulses. The latter propagate to the surface where they are detected at multiple points using either an array of ultrasound transducers or a mechanically scanned single element receiver. By measuring the time of arrival of the acoustic pulses over the tissue surface and, knowing the speed of sound, the acoustic signals can be back-projected in 3D to reconstruct a volumetric image of the internally absorbed optical energy distribution. The fundamental advantage of the technique is that it combines the strong contrast and spectroscopic-based specificity of optical techniques with the high spatial resolution of ultrasound—in particular it avoids the spatial resolution limitations of purely

0003-6935/08/040561-17$15.00/0
© 2008 Optical Society of America

optical imaging techniques due to the overwhelming optical scatter in tissues. As well as providing structural images, functional or physiological information can be obtained by imaging at multiple wavelengths and applying a spectroscopic analysis to quantify the abundance of specific tissue constituents and chromophores; for example, the differences in the spectral characteristics of oxyhemoglobin and deoxyhemoglobin can be exploited to quantify their concentrations and hence the level of oxygenation in the blood [2,3].

Hemoglobin provides the most important source of naturally occurring contrast for photoacoustic imaging. Its relatively strong optical absorption and spectroscopic dependence on oxygenation status makes the technique particularly well-suited to visualizing the structure and function of the vasculature. Applications that exploit this capability include the clinical assessment of tumors such as those in the breast [4,5] and skin [6,7], dermal vascular lesions [8], soft tissue damage such as burns [9], and other abnormalities characterized by changes in local tissue perfusion and oxygenation status. As well as clinical imaging, the technique also has potential as a small animal imaging modality. A variety of studies [10–12] have shown that high-resolution anatomical and functional images of the vasculature in the rat or mouse brain and other organs can be obtained and it has been suggested that, by using targeted optically absorbing contrast agents, the technique may also find application as a molecular imaging modality [12–14].

Currently, most photoacoustic imaging instruments employ piezoelectric receivers to detect the photoacoustic signals. However, these suffer from two specific limitations, particularly for superficial imaging applications. The first relates to the delivery of the excitation laser light. If access to all sides of the target is available, for example, when imaging the small animal brain or the human breast, the detectors can be distributed over a cylindrical [15] or spherical surface [16]. It is then relatively straightforward to deliver the excitation laser light without it being obscured by the detectors—with a cylindrical detection geometry the light can be delivered along the axis of the cylinder and, with a spherical geometry, between individual detectors, assuming a relatively sparsely populated array. However, these detection geometries are not suitable for imaging highly superficial features such as the skin microvasculature, or if strongly echogenic structures such as bone or lung are situated along the acoustic propagation path. Under these circumstances, the so-called backward or reflection mode of operation whereby the photoacoustic signals are detected only on the irradiated side of the tissue is required. Delivering the excitation laser beam now becomes problematic. With a high-density 2D array, there is generally insufficient space between individual detector elements to deliver the light. The obvious solution is to vertically offset the array from the tissue surface, fill the intervening space with an optically transparent acoustic couplant and deliver the laser light obliquely to the tissue surface. However the increased acoustic propagation distance incurred by the acoustic spacer will inevitably reduce the signal-to-noise ratio (SNR) as well as the effective measurement aperture thus reducing image fidelity. Ideally, an optically transparent detector array that can be placed on the tissue surface and the excitation laser pulses transmitted through it and into the underlying tissue is required. Although transparent polyvinylidene fluoride (PVDF) detectors have been fabricated using transparent indium tin oxide (ITO) surface electrodes [17], these remain at an early stage of development and most piezoelectric transducers, and certainly those fabricated from piezoelectric ceramic materials, such as lead zirconate titanate (PZT) and the like, are opaque. The problem of illuminating the tissue is alleviated to some extent if a single mechanically scanned detector, rather than an array of detectors, is employed, assuming that the limitations on acquisition speed associated with mechanical scanning can be tolerated. The light can then be delivered circumferentially around the detector [6], or through the central aperture of a ring-shaped detector [18].

The second limitation of piezoelectric detectors is that the sensitivity falls off with decreasing element size. This can be problematic because most approaches to photoacoustic image reconstruction (Refs. [6] and [19] describe exceptions to this) require that the detector is small compared to the acoustic wavelength so that it approximates to a point receiver. When imaging superficial anatomy (i.e., within a few millimeters of the tissue surface), the photoacoustic signal is only weakly bandlimited by the frequency dependent attenuating characteristics of soft tissues and can therefore be extremely broadband with a frequency content extending to several tens of megahertz. As a consequence, element dimensions of a few tens of micrometers are required and achieving adequate detection sensitivity with piezoelectric receivers of these dimensions then becomes highly problematic.

Optical ultrasound detection techniques may offer the prospect of overcoming these limitations. Their advantage derives from the potential to provide both backward mode detection and significantly smaller element sizes than can be achieved with piezoelectric receivers, in principle down to the optical diffraction limit of a few micrometers. The critical issue then becomes whether they can also provide adequate detection sensitivity given the very low amplitude of photoacoustic signals generated in tissue. Several methods based upon a variety of transduction mechanisms have been investigated or at least proposed for backward-mode photoacoustic imaging. These include a transparent contact sensor based upon the detection of acoustically induced changes in optical reflectance at a glass–liquid interface, the output of which is recorded using a CCD camera [20]. This offers high resolution (<10 μm) but relatively low sensitivity. More sensitive methods employ interferometry. Among these are a noncontact scheme in which a focused laser beam is scanned across the tissue surface and acoustically induced displacements recovered from the phase shifted reflected light using a remote Mach–Zehnder receiving interferometer [21]. A similar approach, in which a remote confocal Fabry–Perot interferometer (FPI) is used to measure displacements across the surface of a pellicle, has also been described [22].

A promising category of interferometric techniques is based upon the detection of acoustically induced changes in the optical thickness of a solid planar FPI—the latter being fabricated by sandwiching a dielectric [23] or polymer spacer [24–27] between a pair of mirrors formed by the deposition of optically reflective coatings. It has been shown that, when using a polymer film as the spacer, this type of sensor can provide broadband frequency responses of the order of several tens of megahertz [25], optically defined element sizes of a few tens of micrometers and, most critically, high sensitivity, comparable to that of broadband piezoelectric receivers [28,29]. Furthermore, by using dichroic dielectric coatings to form the FPI mirrors, the sensor can be made transparent for backward-mode detection [30]. These attributes make this type of sensor well-suited to photoacoustic detection and it has now been implemented in a variety of guises. An early prototype system employed a large area laser beam to illuminate the sensor, an angle-tuned scheme to set the phase bias, and a mechanically scanned photodiode to map the sensor output [31]. This was used to obtain 3D photoacoustic images of a realistic blood vessel phantom and showed that the instrument could provide millimeter penetration depths with spatial resolutions of the order of a few hundred micrometers [32]. Despite demonstrating the underlying feasibility of the concept, inertial limitations associated with mechanical scanning meant that image acquisition time was too long for practical biomedical applications. To overcome this, an alternative sensor readout scheme was subsequently developed [33]. This employed a single focused laser beam that was optically scanned across the surface of the sensor using a high-speed galvanometer-based scanner and the phase bias set by tuning the wavelength of the sensor interrogation laser, an 850 nm vertical-cavity surface-emitting laser (VCSEL). The system was evaluated by mapping the output of various ultrasound transducers in 1D and demonstrated that this type of sensor readout scheme could, in principle, provide the necessary acquisition speed for practical *in vivo* photoacoustic imaging.

In this paper, we describe an instrument based on the latter approach but incorporating several key technical developments and evaluated specifically for the purpose of photoacoustic imaging. These developments include the addition of a second galvanometer so that the sensor output can be mapped in 2D and the use of a new sensor design in which the FPI mirrors are transparent over an extended range in the near infrared (600–1200 nm). The latter enables the system to operate in backward mode over the wavelength range that tissue is relatively transparent. In addition, a 1550 nm *C–L* band external cavity laser is now used as the sensor interrogation laser resulting in a significant increase in detection sensitivity due to its low noise characteristics and high output power. As well as these developments, the system has been evaluated extensively by imaging various tissue mimicking phantoms. The underlying feasibility of the concept has been reported in a preliminary account [34,35]. In the current paper a detailed description of the operating principles of the instrument, its performance, and application to high-resolution biomedical photoacoustic imaging is provided. Subsections 2.B and 2.C describe the Fabry–Perot (FP) sensor head and the sensor readout scheme, respectively. Subsection 2.D describes the performance of the system in terms of the spatial scan parameters, acquisition time, and the acoustic performance. In Subsection 3.A, measurements of the line-spread function (LSF) of the instrument are discussed and in Subsection 3.B images of a range of tissue mimicking phantoms are presented.

2. Backward-Mode Photoacoustic Scanner

A. Overview

The principles of operation of the scanner are as follows. A tunable excitation laser system provides nanosecond visible or NIR optical pulses for generating the photoacoustic waves. The latter are detected over the surface of the tissue using a 2D optical ultrasound field mapping system, the acoustically sensitive element of which is a planar FP polymer film sensing interferometer (FPI). A key feature of the system is that it operates in backward mode. This is made possible by designing the mirrors of the FPI to be transparent to the excitation laser wavelength but highly reflective at others. This allows the sensor head to be placed in acoustic contact with the tissue surface and the excitation laser pulses transmitted through it and into the underlying tissue. The resulting photoacoustic waves propagate back to the surface where they modulate the optical thickness of the FPI and hence its reflectivity. By scanning a cw focused laser beam (at a wavelength at which the FPI mirrors are highly reflective) across the surface of the sensor and recording the time-varying reflected optical power modulation at each point of the scan, the spatial-temporal distribution of the incident photoacoustic waves can be mapped in 2D. The detected photoacoustic signals are then input to a k-space acoustic backpropagation algorithm in order to reconstruct a 3D image of the initial pressure distribution: the photoacoustic image.

In Subsections 2.B–2.D, a detailed description of the scanner hardware, operating principles, and performance is provided. The design and fabrication of the FP sensor is detailed in Subsection 2.B. The optical scanning system and interrogation scheme required to map the sensor output are described in Subsection 2.C while the performance of the system in terms of the spatial scan parameters, acquisition speed, and acoustic performance are outlined in Subsection 2.D. An overview of the image reconstruction algorithm is provided in Subsection 2.E.

B. Fabry–Perot Sensor Head: Design and Fabrication

The FP sensor head design and the method of fabrication are broadly similar to that described previously [30], the principal difference being that the spectral band over which the FPI mirrors are highly transmissive has been shifted from 1050–1400 nm to 590–1200 nm. This offers two advantages. First, the FPI mirrors now exhibit high transmittance over a wavelength range that coincides with the so-called NIR window (600–1000 nm) for biological tissues. This allows the sensor head to be transparent, and therefore operate in backward mode, over this important wavelength range. Second, it allows the sensor interrogation wavelength, at which the mirrors are required to be highly reflective, to be shifted from 850 to ~1550 nm. This enables the relatively inexpensive, widely tunable, and robust *C–L* (1516–1610 nm) band lasers originally developed for optical telecommunications applications to be used as the sensor interrogation laser source.

A schematic of the sensor head is shown in Fig. 1. It comprises a wedged polymethylmethacrylate (PMMA) backing stub onto which a thin polymer (Parylene C) film spacer sandwiched between two dielectric dichroic mirrors is deposited in order to form the FPI. The fabrication procedure comprises the following four steps.

1. The first FPI dichroic mirror is formed by sputtering a stack of alternate $\lambda/4$ thick layers of ZnS and Na_3AlF_6 on to the backing stub. This results in an eight-layer structure of total thickness 1.885 μm. The mirror is of a short pass filter design, the spectral characteristics of which are shown in Fig. 2. This shows that the coating is highly transmissive between 600 and 1200 nm, termed the excitation passband, but highly reflective (>95%) between 1500 and 1650 nm, the sensor interrogation band.
2. A Parylene C polymer film spacer of refractive index $n = 1.65$ and of thickness either 38 (as shown in Fig. 1) or 22 μm is vacuum deposited onto the dielectric coating. This process involves forming a monomer gas from a dimer precursor and introducing it into a vacuum chamber held at room temperature that contains the substrate [36]. The monomer gas then condenses and polymerizes on the substrate forming a conformal transparent coating.
3. A second dichroic dielectric coating, of an identical design to the first, is deposited on top of the Parylene spacer to form the second FPI mirror.
4. Finally, a 12 μm thick Parylene C barrier coating (not shown in Fig. 1) is deposited over the entire structure to protect the external FPI mirror from damage due to abrasion or water ingress.

The above procedure was used to fabricate two sensors, one with a 38 μm thick spacer as shown in Fig. 1, the other with a 22 μm spacer. A photograph of a typical sensor is shown in Fig. 3. The free spectral range (FSR) of the sensor with the 38 μm thick spacer is 18.8 nm, the reflectivity finesse $F_R = 34.8$, and the visibility $V = 0.66$. For the sensor with the 22 μm spacer the FSR = 31.4 nm, $F_R = 42.4$, and $V = 0.8$.

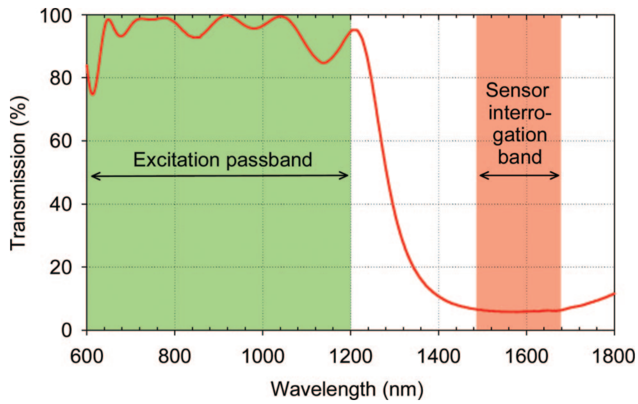

Fig. 2. (Color online) Transmission characteristics of the dichroic dielectric coatings used to form the mirrors of the FPI. The coatings provide the high reflectivity (95%) required to form a high-finesse FPI between 1500 and 1650 nm (the sensor interrogation band) but are highly transmissive between 600 and 1200 nm (the excitation passband) enabling photoacoustic excitation laser pulses in this wavelength range to be transmitted through the sensor.

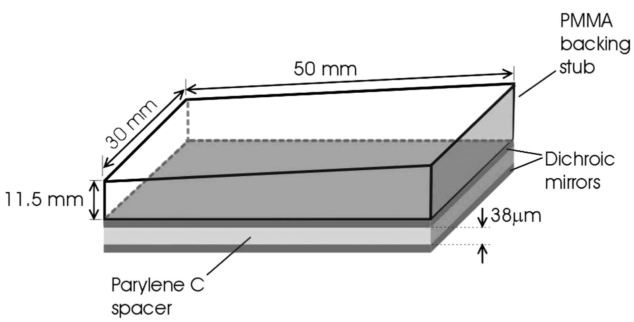

Fig. 1. Schematic of FP sensor head. The sensing structure comprises a 38 μm polymer (Parylene C) film spacer sandwiched between two dichroic mirrors forming an FPI. The latter overlays a PMMA backing stub that is wedged to eliminate parasitic interference between light reflected from its upper surface and the FPI.

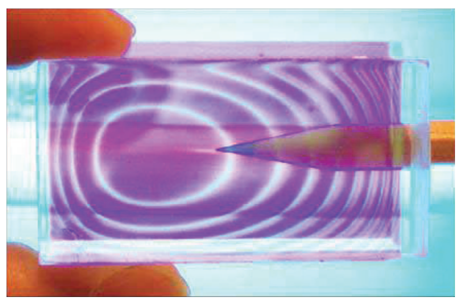

Fig. 3. (Color online) Photograph of sensor head shown in Fig. 1 (wedge side uppermost) under narrowband visible illumination showing concentric elliptical FPI transmission fringes and the transparent nature of the sensor head.

There are several advantages of the fabrication process outlined above. The use of a gas phase deposition process to form the polymer film spacer provides a highly conformal coating with excellent surface finish and uniformity of thickness (<5 nm over an area of 1 cm^2). These attributes enable a high-quality FPI with good fringe visibility and finesse to be produced. The thickness can also be precisely controlled (<0.1 μm) to design sensors with specific FSRs and acoustic bandwidths. Furthermore, the use of all vacuum deposition methods allows for the inexpensive batch fabrication of large quantities of sensors with high repeatability.

C. System Design and Operating Principles

A schematic of the system is shown in Fig. 4. Nanosecond laser pulses at a wavelength within the sensor excitation passband (600–1200 nm) are incident on the FP sensor head and transmitted through it into the target beneath it. Absorption of the laser energy produces photoacoustic pulses that propagate back to the sensor head. The sensor is read-out by raster scanning a 1550 nm focused interrogation laser beam over its surface using an *x–y* optical scanner and detecting the reflected beam with a photodiode. At each point of the scan, the sensor is optimally biased by tuning the interrogation laser wavelength to the point of maximum slope on the FP interferometer transfer function (ITF), the relationship between the reflected optical power and phase. Under these conditions, the transduction mechanism can be regarded as one in which an acoustically induced modulation of the optical thickness of the FPI produces a small phase shift that is linearly converted, via the ITF, to a corresponding reflected optical power modulation. By mapping the sensor output in this way, the 2D distribution of acoustic waves incident on the surface of the sensor can be recorded. The entire system is fully automated with the excitation and interrogation lasers, the optical scanner, and the data acquisition hardware all under the control of a PC. Details of the key elements of the system, the exci-

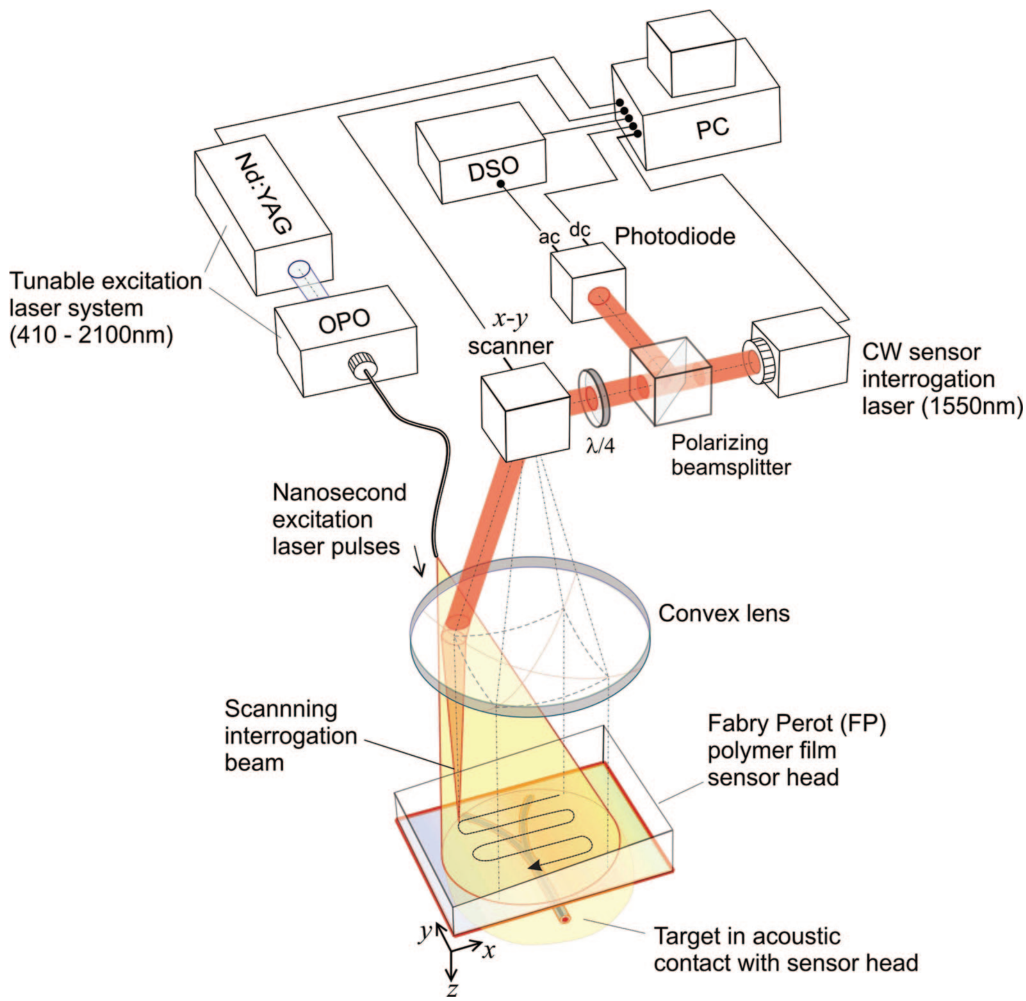

Fig. 4. (Color online) Backward-mode multiwavelength photoacoustic scanner. A tunable OPO laser system provides nanosecond optical pulses for exciting the photoacoustic waves within the target, which is placed underneath and in acoustic contact with the FP sensor head. A second laser operating at 1550 nm provides a focused interrogation laser beam that is raster scanned over the surface of the sensor to map the incident photoacoustic waves.

tation source, the optical scanning system, phase bias control scheme, and the data acquisition system are provided below.

1. *Excitation Source*

One of two fiber-coupled excitation sources was available to generate the photoacoustic signals. The first (shown in Fig. 4) was a type I optical parametric oscillator (OPO)(GWU VisIR) pumped by the 355 nm frequency tripled output of a *Q*-switched Nd:YAG laser (Spectra-Physics, Quanta Ray LAB170). This system is capable of providing 8 ns optical pulses over the wavelength range 410–2100 nm with end-of-fiber pulse energies in the range 12–36 mJ (depending on wavelength) at a pulse repetition frequency (PRF) of 10 Hz. The second excitation source was a *Q*-switched Nd:YAG laser (Big Sky, Ultra) operating at 1064 nm. This provided a shorter pulse duration of 5.6 ns and a higher pulse energy and PRF of 45 mJ and 20 Hz, respectively.

2. *Scanning System*

A 10 mW fiber-coupled tunable cw external cavity laser (Thorlabs ECL5000DT) operating at a nominal wavelength of 1550 nm was used to provide the sensor interrogation beam. The beam was focused using a lens onto the surface of the sensor at normal incidence and optically scanned across it using an x–y scanner comprising a pair of mutually orthogonal closed loop galvanometer mirrors; in essence a 2D version of the scanner described in [33]. The beam reflected from the sensor is directed via a polarizing beam splitter onto a 50 MHz InGaS photodiode–transimpedance amplifier configuration with dc- and ac-coupled outputs. The dc-coupled output is connected to a 200 Ks/s 16-bit analog-to-digital (A/D) card within the PC and used to record the ITF as required for the phase bias control procedure described in Subsection 2.C.3. The ac-coupled output (-3 dB cutoff frequency: 100 kHz) is connected to a 300 MHz digitizing oscilloscope (DSO) and used to record the time-varying reflected optical power modulation produced by the incident acoustic wave. The reason the photodiode output is ac coupled is to remove the large dc optical component reflected from the sensor and low-frequency fluctuations in the output power of the interrogation laser. Once the photoacoustic signal has been acquired by the DSO it is downloaded to the PC via an IEEE 488 general purpose interface bus (GPIB).

3. *Phase Bias Control Scheme*

To obtain maximum sensor sensitivity, it is necessary to optimally bias the FPI by tuning the interrogation laser wavelength so that it corresponds to the point of maximum slope on the ITF. This biasing procedure must be performed at each point of the x–y scan since the optical thickness of the polymer film spacer, and therefore the optimum bias wavelength, varies from point to point. To determine the optimum bias wavelength, the laser wavelength is first swept over a range that is greater than the FSR of the FPI while

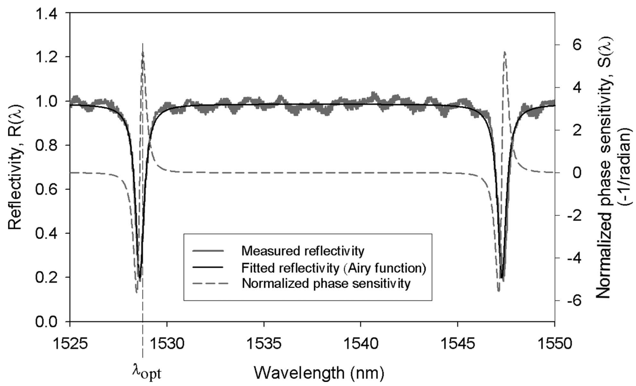

Fig. 5. Reflectivity $R(\lambda)$ and normalized phase sensitivity $\bar{S}(\lambda)$ as function of wavelength for the 38 μm FP sensor. The optimum bias point of the sensor is the wavelength λ_{opt} at which $\bar{S}(\lambda)$ is a maximum. At this wavelength the reflected optical power modulation due to an acoustically induced phase shift is a maximum and the sensor is said to be optimally biased.

monitoring the reflected optical power via the dc-coupled output of the photodiode. This provides the wavelength dependent reflectivity transfer function $R(\lambda)$; an example of which is shown in Fig. 5. To obtain a noise-free $R(\lambda)$, an Airy function (the solid dark curve in Fig. 5) is fitted to the measured data. The reflectivity R is then expressed as a function of phase thus providing the normalized ITF, the derivative of which is then computed. This derivative is plotted as a function of the wavelength in Fig. 5 and is termed the normalized phase sensitivity $\bar{S}(\lambda)$: it represents the sensitivity of the sensor to an acoustically induced phase shift as a function of operating wavelength. The laser wavelength is then set to λ_{opt}, the value that corresponds to the maximum value of $\bar{S}(\lambda)$ and therefore the highest sensitivity. At this wavelength, the sensor is said to be optimally biased. The time taken to bias the FPI depends on the variation of λ_{opt} from one spatial point to the next but is, on average, less than 50 ms.

4. *Signal Acquisition and Processing*

To acquire a photoacoustic signal, the interrogation laser beam is first positioned at some initial point on the sensor. Once the wavelength has been set to λ_{opt}, in order to optimally bias the sensor as described in Subsection 2.C.3, the excitation laser is fired. At the same time, the DSO is triggered in order to begin acquiring the photoacoustic waveform. Once the acquisition is complete, the waveform is downloaded to the PC where it is divided by the value of $\bar{S}(\lambda)$ obtained for that spatial point in order to compensate for sensitivity changes due, for example, to spatial variations in the reflectivities of the FPI mirrors, defects in the Parylene film spacer, or fluctuations in the laser output power between acquisitions. The interrogation laser beam is then moved to the next scan point and the process repeated until the scan is complete. Thus, for a 2D scan, the recorded data set is a 3D array $p(x, y, t)$, representing the distribution of the incident time-varying acoustic pressure p over the x–y detection plane. This data set is then used to reconstruct a 3D image as described in Subsection 2.E.

D. System Performance

In Subsections 2.D.1–2.D.6 the performance of the detection system is described in terms of the essential parameters required to specify an ultrasound field mapping system: namely, the dimensions and spatial sampling intervals of the acoustic aperture, acquisition speed, and the acoustic performance in terms of detection sensitivity, linearity, frequency response, and effective element size.

1. *Scan Parameters: Scan Area, Step Size, and Spot Size*

The maximum dimensions over which the interrogation laser beam can be scanned over the sensor is defined by a circle of diameter 50 mm—that is to say the area over which the photoacoustic signals are to be mapped must lie within this circle. The diameter of the laser beam at its focus, the $1/e^2$ spot size, is 64 μm and the minimum step size (limited by the 12-bit resolution of the PC digital-to-analog conversion (D/A) card that controls the optical scanner) is 10 μm.

2. *Acquisition Speed*

The acquisition time per scan step is approximately 1 s. This is dominated by a combination of the time taken to rearm the DSO between acquisitions and the download time from the DSO to the PC via the GPIB interface for each acquisition. As described further in Section 4, this could be significantly reduced through the use of an alternative acquisition scheme in which all of the waveforms acquired over the scan are stored within the on-board memory of the digitizer (in this case the DSO) and downloaded in a single step to the PC hard drive. This would offer the prospect of achieving an acquisition speed limited by the PRF of the excitation laser.

3. *Detection Sensitivity*

The detection sensitivity or noise-equivalent pressure (NEP) is defined as the acoustic pressure that provides a system SNR of unity in the low-frequency limit [25] $\lambda_a \gg l$ where λ_a is the acoustic wavelength and l is the FPI thickness. The NEP therefore represents the minimum detectable acoustic pressure and is given by

$$\mathrm{NEP} = \frac{N}{S_o},$$

where S_o is the sensor sensitivity and is defined as the reflected optical power modulation per unit acoustic pressure (μW/MPa) at the optimum bias point of the FPI [25]. S_o is proportional to the phase sensitivity (as defined in Subsection 2.C.3) and therefore depends on the incident optical power and the shape of the ITF, which in turn depends on the reflectivities of the FPI mirrors and the phase dispersion imposed by the geometry of the laser beam and nonuniformities in the thickness of the polymer film spacer. S_o also depends on the thickness and elastic and photoelastic properties of the polymer film and the acoustic impedance of the backing stub [25]. N is the minimum detectable optical power modulation reflected from the sensor over a specified measurement bandwidth and is a function of the noise characteristics of the laser source and the photodiode–transimpedance amplifier configuration. For the specific system reported in this paper, the noise is dominated by the latter.

To determine S_o, the reflected optical power modulation produced by the output of a pulsed 3.5 MHz PZT ultrasound source that had been previously calibrated using a PVDF membrane hydrophone was measured. To obtain N, the peak output noise voltage of the photodiode was measured over a 20 MHz bandwidth and converted to an equivalent optical power. Note that peak rather than rms noise figures are quoted as the former provides a more realistic indication of the smallest signal that can be detected when measuring broadband signals in the time domain. From the measurements of N and S_o, the peak NEP was found to be 0.21 kPa for the 38 μm sensor and 0.31 kPa for the 22 μm sensor. In both cases the measurement bandwidth was 20 MHz. Note that in this case the NEP of the two sensors is not in direct proportion to their thicknesses as might be expected because the 22 μm sensor has a higher visibility and finesse compared to the 38 μm sensor as noted in Subsection 2.B.

Although it has been suggested that optical ultrasound sensors are, in general, significantly less sensitive than conventional piezoelectric transducers [37], this is not the case with the FP sensor. It depends critically upon the element size under consideration. The NEP values quoted above are comparable to that of a 1 mm diameter piezoelectric PVDF receiver [29] terminated with a high-quality preamplifier. Indeed, if the more appropriate comparison is made between a PVDF receiver of similar element size to that of the FP sensor, it becomes evident that the latter is much more sensitive. For example, a 75 μm diameter PVDF receiver can be expected to have a typical NEP of around 50 kPa [28] and is therefore more than 2 orders of magnitude less sensitive than the FP sensor that, in this study, has an optically defined active diameter of 64 μm.

4. *Linearity*

Assuming the elastic limits of the polymer film are not exceeded, the upper limit of linear acoustic detection is determined by the phase range over which the ITF is linear and the acoustic phase sensitivity. The later is defined as the magnitude of the optical phase shift produced per unit acoustic pressure [25]. For the 38 μm sensor, the linear phase range (to within 10%) around the optimum bias point was measured to be 0.039 rad. Using a value for the acoustic phase sensitivity of 0.03 rad/MPa (based on a previously reported value of 0.15 rad/MPa for a 50 μm thick rigid-backed Parylene sensor film illuminated with light at 850 nm [28]), this corresponds to an upper limit of linear detection of 1.3 MPa. The corresponding value for the 22 μm sensor is 1.8 MPa. In general, the peak pressures of photoacoustic signals generated in tissues are of the order of kilopascals and therefore well within the linear operating range of both sensors.

5. *Frequency Response*

Assuming the sensor operates predominantly in thickness mode, the bandwidth for a normally incident plane wave is determined by the thickness and speed of sound of the polymer film and the acoustic impedance of the backing material. The uniformity of response is determined by the acoustic impedance mismatches at the boundaries of the film, on one side due to the backing, on the other due to the surrounding coupling medium, usually water. In general, polymer films have an acoustic impedance close to water, and uniform broadband response characteristics can therefore be expected. This can be seen in Fig. 6, which shows the predicted and measured frequency responses of the two sensors used in this study. The predicted response was obtained using an analytic model that calculates the frequency dependent mean distribution of stress across the polymer film thickness by the summation of acoustic reflections within the film [25]. This model has been experimentally validated previously using sensors in which gold or aluminium coatings were used to form the FPI mirrors [25]. Since these coatings are typically only a few tens of nanometers thick they can be regarded as being acoustically negligible as required by the model. However, the dielectric coatings used to form the mirrors in the sensors used in this study are significantly thicker (~2 μm). Measurements of the frequency response were therefore made to check that the model was still valid for these sensors. The experimental method was similar to that described in [25] in which a broadband acoustic pulse was generated by the absorption of nanosecond laser pulses in a strong absorber. The acoustic pulse was detected first with a 10 μm thick FP sensor of known frequency response characteristics (−3 dB bandwidth of 88 MHz) that acted as a reference sensor and then by each of the two sensors. The detected waveforms were Fourier transformed and the frequency responses of the two sensors under test were obtained by taking the ratio of the acoustic spectrum of each sensor to that of the reference sensor. As Fig. 6 shows, the measured and predicted responses are in close agreement with a smooth roll-off to zero (where $\lambda_a = l$) at 57.9 MHz for the 38 μm sensor and 100 MHz for the 22 μm sensor. Note that the −3 dB bandwidth for the 38 μm sensor is 22.2 MHz and therefore approximately 20% less than the sensor described in [33], which is of the same thickness but fabricated using a polycarbonate rather than PMMA backing. This is a consequence of the greater acoustic impedance mismatch between PMMA and Parylene, which modifies the shape of the frequency response curve in such a way that the −3 dB bandwidth is reduced, although the position of the minimum remains the same at 57.9 MHz.

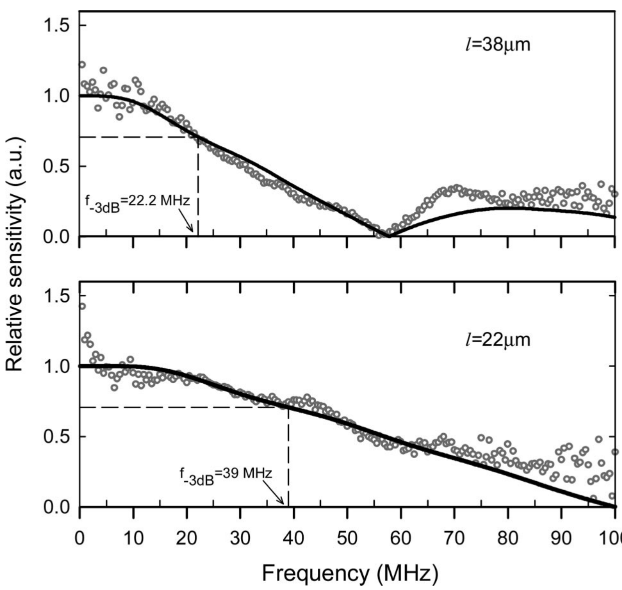

Fig. 6. FP sensor frequency response. Predicted (solid curves) and measured (circles) responses for the two sensor thicknesses used in this study: $l = 38$ μm (top) and 22 μm (bottom).

6. *Effective Acoustic Element Size*

The dimensions of the interrogation laser beam at its focus defines, to a first approximation, the dimensions of the acoustically sensitive region of the sensor, also called the effective acoustic element size as defined in [38]. However there will clearly be some limit to this assumption. If the laser beam spot diameter d is progressively reduced, one might expect that the effective acoustic element diameter d_{eff} will eventually attain a minimum limiting value beyond which it cannot be reduced further, no matter how small d becomes. A further expectation might be that this limiting value of d_{eff} will decrease as the thickness of the polymer film spacer l is reduced. These intuitive assertions are supported by a study in which an analytic model [38] that solves the acoustic wave equation for each of the different layers of the sensor was used to simulate the directional response of the sensor and from this obtain d_{eff} as function of d and l. Using this model, it was found that, for the spot diameter $d = 64$ μm used in the current study, the effective diameter d_{eff} for the 38 μm sensor is $d_{\mathrm{eff}} = 90$ μm and for the 22 μm sensor, $d_{\mathrm{eff}} = 70$ μm. Thus, in this case the spot size and effective element size are the same only for the 22 μm sensor. In general, it was found that, providing the laser beam diameter is significantly larger than the thickness of the polymer film (by say a factor of 2–3), the optically defined element size and effective element size can be taken to be the same. This raises the question as to what the smallest achievable value of d_{eff} might be. This was found to be given by $d_{\mathrm{eff}} = 1.8l$ and to obtain this limiting value it is required that $d < l/2$. So, for the 38 μm sensor it would be possible to achieve a minimum value of $d_{\mathrm{eff}} = 68.4$ μm by illuminating with a spot diameter of 19 μm. For the 22 μm sensor, the minimum $d_{\mathrm{eff}} = 39.6$ μm and would require illuminating with an 11 μm spot diameter. To achieve a smaller d_{eff} would require reducing l. All of this suggests that while it is often reasonable to assume that the optically defined element size and effective element size are the same, it is not always so, particularly when the interrogation laser beam dimensions begin to approach the sensor thickness.

E. Image Reconstruction Algorithm

The image reconstruction algorithm recovers a 3D image of the initial pressure distribution $p_o(x, y, z)$, from the time-resolved photoacoustic signals $p(x, y, t)$ recorded over the surface of the sensor. The assumption then is that $p_o(x, y, z)$ can be taken to be proportional to the absorbed optical energy density assuming impulsive deposition of the laser energy.

The reconstruction algorithm is based on an analytic inverse k-space method that is applicable to planar [39] and linear detection geometries [40]. This approach is based upon the premise that the spatial frequency components of $p_o(x, y, z)$ are directly mapped on to, and can therefore be recovered from, the spatial and temporal frequency components of the set of detected pressure signals $p(x, y, t)$. The derivation and computational implementation of this method is described in detail for 2D and 3D domains in references [40] and [39], respectively. In brief however, for a 3D reconstruction, it requires (1) taking a 3D Fourier transform of the detected photoacoustic signals $p(x, y, t)$ to obtain $p(k_x, k_y, \omega)$, where k_x and k_y are the x and y spatial frequencies in the sensor plane and ω is the temporal frequency; (2) mapping ω to the vertical spatial frequency k_z using the dispersion relationship $\omega = c\sqrt{k_x^2 + k_y^2 + k_z^2}$ to obtain the spatial frequency components of the initial pressure distribution $p_o(k_x, k_y, k_z)$; and (3) inverse Fourier transforming $p_o(k_x, k_y, k_z)$ to obtain the required initial pressure distribution $p_o(x, y, z)$. The advantage of this approach over time domain back projection methods for planar detection geometries is that it is significantly faster, typically by several orders of magnitude due to the computational efficiencies gained through the use of the fast Fourier transform (FFT).

3. System Evaluation

The system has been evaluated by imaging various absorbing structures immersed in a scattering liquid. The purpose of these experiments was threefold: (1) to estimate the spatial resolution that the system could provide, (2) to show that the system can provide accurate 3D images of arbitrarily shaped absorbers, and (3) to demonstrate that a physiologically realistic tissue phantom designed to represent a network of blood vessels could be imaged. All experiments were undertaken in backward mode, no signal averaging was used, and the incident fluence of the excitation laser pulses was always less than 15 mJ/cm^2 and thus below the maximum permitted exposure (MPE) for skin [41]. No filtering or processing of the reconstructed images was undertaken.

A. Instrument Line-Spread Function

To obtain a measure of the spatial resolution that the system can provide, measurements of the instrument LSF were made. This was achieved by imaging a target comprising six rows of highly absorbing polymer ribbons using the experimental arrangement shown in Fig. 7. The thickness of the ribbons was approximately 30 μm, the length 25 mm, and the widths were in the range of 80–120 μm for the lower five rows and approximately 300 μm for the top row. The target was immersed in an optically scattering liquid (an aqueous solution of Intralipid of reduced scattering coefficient $\mu_s' = 1\ \mathrm{mm}^{-1}$) to homogenize the light distribution and placed parallel to the detection plane with the length of the ribbons aligned parallel to the y axis. The excitation laser beam was transmitted through the sensor and into the target. The sensor interrogation beam was scanned along a line of length 40 mm in steps of 20 μm in the x direction and the time dependent photoacoustic signals recorded at each step of the scan. A typical example of the set of measured photoacoustic signals $p(x, t)$ obtained using the OPO as the excitation source and the 22 μm FP sensor is shown in Fig. 8(a). Figure 8(b) shows the image of the initial pressure distribution $p_o(x, z)$ reconstructed from the data in Fig. 8(a) using the 2D Fourier-transform algorithm [40] referred to in Subsection 2.E. To view the deeper lying ribbons, a depth dependent exponential scaling factor was applied to the reconstructed image to compensate for the light attenuation. The lateral and vertical LSFs were obtained from the dimensions of the reconstructed features in Fig. 8(b) using the method described below.

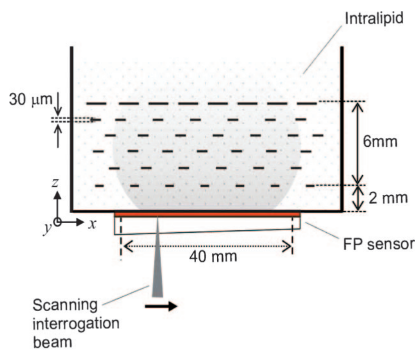

Fig. 7. (Color online) Experimental arrangement for measuring the instrument LSF. The target is a matrix of highly absorbing discrete polymer ribbons, immersed in Intralipid ($\mu_s' = 1\ \mathrm{mm}^{-1}$), and aligned parallel to the detection plane. The excitation laser beam (not shown) is transmitted through the sensor into the target. The photoacoustic signals emitted by the target are mapped by scanning the sensor interrogation beam along a line of length 40 mm in steps of 20 μm in the x direction.

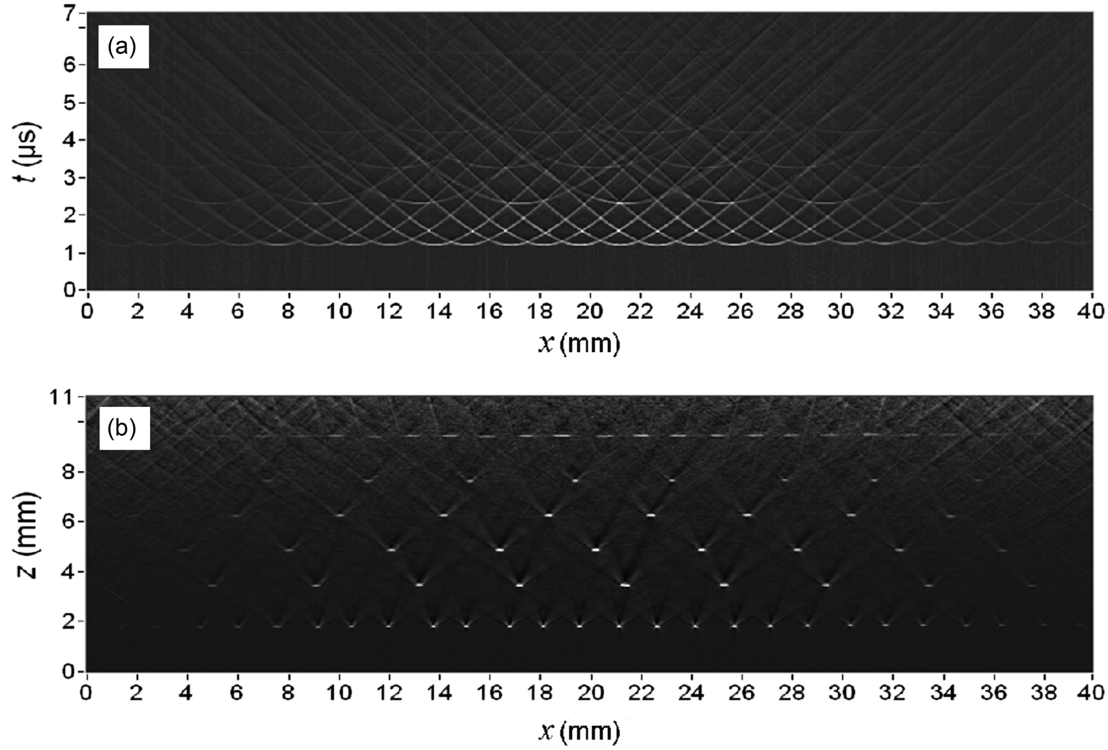

Fig. 8. (a) Map of photoacoustic signals $p(x, t)$ generated in the target shown in Fig. 7. Line scan length $x = 40$ mm, step size $dx = 20$ μm, spot diameter $d = 64$ μm, temporal sampling interval $dt = 4$ ns, incident fluence $\Phi = 2$ mJ/cm^2, and pulse duration $t_p = 8$ ns. (b) Two-dimensional photoacoustic image of initial pressure distribution $p_o(x, z)$ reconstructed from $p(x, t)$.

1. *Lateral Line-Spread Function*

Due to the practical difficulties involved in cutting the absorbing ribbons with small enough lateral dimensions (a few tens of micrometers) to approximate to a spatial delta function in the x direction, the width of the ribbons was deliberately chosen to be significantly greater than the minimum expected lateral LSF (i.e., the LSF in the x direction). The ribbons could therefore be regarded as providing a step function in the x direction. This enabled the edge-spread function (ESF) to be estimated from the boundaries of the reconstructed features in Fig. 8(b) and the LSF obtained by taking the spatial derivative of the ESF. This method is illustrated in Fig. 9, which shows an expanded view of one of the reconstructed features in the second row of Fig. 8(b). A horizontal profile at $z = 3.45$ mm is taken through the center of the feature and Lorentzian functions fitted to the rising and falling edges of the profile in order to remove the noise due to the discretization in the reconstruction. The rising edge of the fit is taken as the ESF. The derivative of the ESF is then computed and the lateral LSF is given by the full width at half-maximum (FWHM) of the peak of the derivative.

The LSFs were obtained in this way for each feature in the reconstructed image in Fig. 8(b) to enable the variation of the lateral LSF over the image plane to be determined. This is illustrated in the contour plots of Fig. 10, which show the x–z dependence of the lateral LSF for the two sensors—these data were obtained using the Q-switched Nd:YAG as the excitation source. As expected, the lateral LSF is spatially variant. For example, for the 22 μm sensor, the LSF increases with depth from 38 μm at $z = 2$ mm to 66 μm at $z = 5$ mm at the center of the line scan. It also increases with horizontal distance from the center of the scan ($x = 20$ mm); for example, at a distance of 10 mm from the center of the scan the LSF increases by a factor of approximately 1.6. In both cases, the increased LSF occurs because a

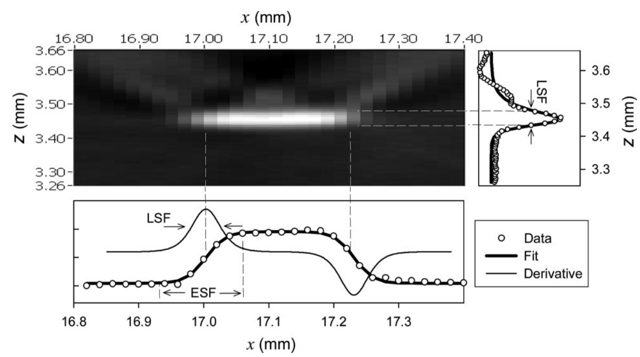

Fig. 9. Estimation of instrument LSF. Image (top) shows an expanded view of the feature at $x = 17.10$ mm and $z = 3.45$ mm in Fig. 8(b). A horizontal profile through the center of the feature ($z = 3.45$ mm) is shown below. The rising edge of the profile represents the edge spread function (ESF) and the lateral LSF is given by the FWHM of the derivative of the ESF. The vertical LSF is obtained from the FWHM of the vertical profile through the center ($x = 17.10$) of the feature (shown right).

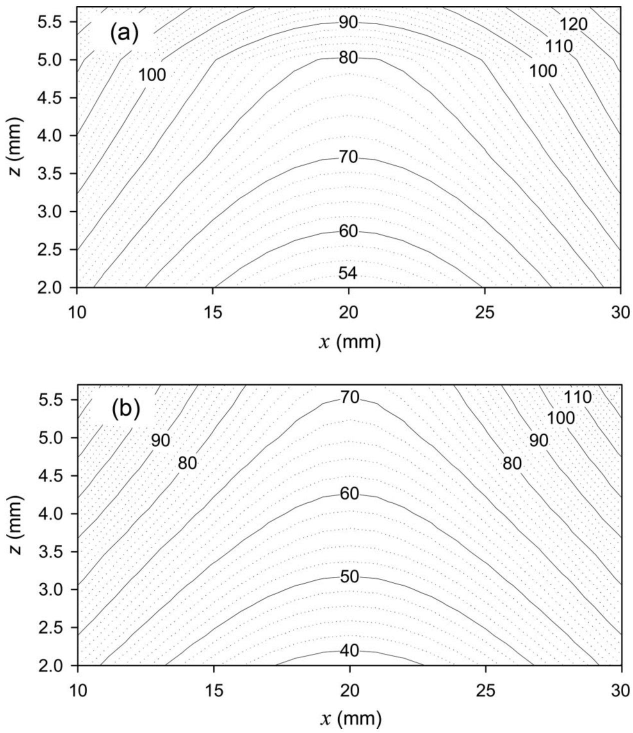

Fig. 10. Contour plots showing x–z dependence of lateral LSF (in micrometer) for (a) 38 and (b) 22 μm sensor. Laser pulse duration = 5.6 ns.

smaller proportion of the emitted wavefront is captured, so the effective measurement aperture is reduced thus reducing the data available to the reconstruction algorithm.

In general, the lateral LSF is influenced by a variety of instrument related parameters. These include the overall detection aperture (the length of the line scan), the effective element size, spatial sampling interval, and the bandwidth of the sensor. The influence of the last of these is evidenced by the significantly smaller lateral LSF obtained with the 22 μm sensor. In addition, the laser pulse duration influences the frequency content of the photoacoustic signal and therefore the LSF. Given the large detection aperture (40 mm), the small step size (20 μm), and the short laser pulse duration (5.6 ns), it is suggested that the finite effective element size is the most likely limiting parameter. If the detector does not act as a point detector, it does not provide a truly omnidirectional response. It is therefore unable to receive signals incident at large angles thus reducing the effective overall detection aperture and increasing the LSF.

2. *Vertical Line-Spread Function*

Obtaining a realistic measurement of the vertical LSF proved to be less straightforward than measuring the lateral LSF. The thickness of the absorbing ribbons (~30 μm) is not large enough to approximate to a step function to enable the LSF to be estimated from the ESF as described above nor small enough to approximate to a spatial delta function in the z direction and thus provide the LSF directly. The latter is evidenced by the fact that the FWHM thicknesses of the reconstructed ribbons (estimated as shown in Fig. 9) were found to be approximately 40 μm for the 38 μm sensor and 32 μm for the 22 μm sensor. It is suspected that these values are limited by the finite thickness of the target and are therefore significant overestimations of the true LSF. The rationale for this suggestion is as follows. Unlike the lateral LSF the vertical LSF is, to a first approximation, spatially invariant and defined largely by the bandwidth of the detector, which is a function of the thickness of the polymer film spacer l. By considering the transit time of an acoustic impulse across the sensor, it can be shown that the vertical LSF is given by the acoustic thickness of the sensor: the product of the physical thickness l and the ratio of the sound speed in water (1500 m/s) to that in the Parylene spacer (2200 m/s). By this reasoning, the vertical LSFs for the 38 and 22 μm sensors should be 26 and 15 μm, respectively; significantly lower than the measured values referred to above.

To establish whether these estimates are reasonable, a 10 mm thick slab of PMMA with a thin layer of ink on one side (applied using a felt tip pen) was used as an absorbing target. It is assumed that the thickness of the ink is no more than a few micrometers. It is therefore much thinner than the absorbing ribbons and can reasonably be assumed to approximate to a spatial delta function in the z direction. The PMMA slab was positioned with the ink layer face down and parallel to the plane of the sensor at a vertical distance of 1.5 mm from it. It was irradiated with a 20 mm diameter beam provided by the Q-switched Nd:YAG laser producing a plane wave that was normally incident on the sensor: the sensor interrogation beam was aligned with the axis of the excitation laser beam. The large lateral dimensions of the source are such that the inverted edge waves originating from its perimeter are sufficiently time delayed with respect to the initial plane wave that they can be time-gated out. The temporal waveform recorded by the sensor is therefore a monopolar pulse. The product of the FWHM of this pulse with the speed of sound in water provides the "reconstructed" thickness of the target, which is taken to be the vertical LSF. Using this method, the vertical LSF for the 38 μm sensor was found to be 27 μm and the LSF for the 22 μm sensor was 19 μm. Both values are considered to be more realistic indications of the vertical LSF and consistent with the predicted values based upon the acoustic thickness of the sensors described above. The value for the 22 μm sensor is slightly higher than expected because the higher bandwidth of this sensor means that the 5.6 ns laser pulse duration now becomes the limiting factor.

B. Three-Dimensional Imaging of Arbitrary Shaped Absorbers

To demonstrate the ability of the system to provide 3D images of absorbing objects of arbitrary geometry, a range of phantoms composed of well-defined ab-

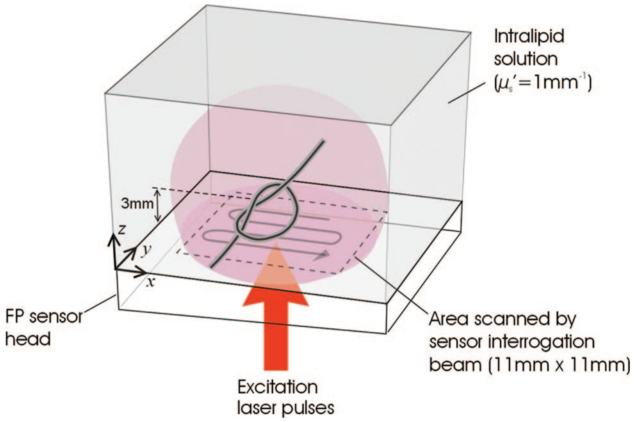

Fig. 11. (Color online) Arrangement of dye-filled knotted tube with respect to the FP sensor head. The tube is immersed in Intralipid ($\mu_s{}' = 1\ \text{mm}^{-1}$) and positioned approximately 3 mm above the detection plane.

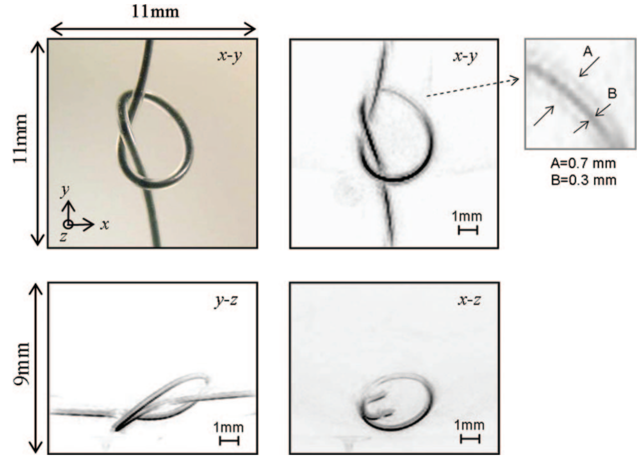

Fig. 12. (Multimedia online; ao.osa.org) (Color online) Photoacoustic images of dye-filled knotted tube (inner diameter = 0.3 mm, outer diameter = 0.7 mm, $\mu_a > 10\ \text{mm}^{-1}$) immersed in Intralipid ($\mu_s{}' = 1\ \text{mm}^{-1}$) using the arrangement shown in Fig. 11. Top left: photograph of tube prior to immersion in Intralipid. Top right: x–y maximum intensity projection (MITP) of 3D photoacoustic image. Lower left: y–z MITP, lower right: x–z MITP, far right: close-up of x–y MITP showing that the dye-filled lumen can be distinguished from the outer wall of the tube. Scan area = 11 mm × 11 mm, step size dx = dy = 100 μm, spot diameter d = 64 μm, temporal sampling interval dt = 20 ns, incident laser fluence Φ = 12 mJ/cm^2, λ = 1064 nm, and pulse duration t_p = 5.6 ns.

sorbing structures immersed in an optically scattering liquid, an aqueous solution of Intralipid ($\mu_s{}' = 1\ \text{mm}^{-1}$), were imaged. One of these phantoms was a silicone rubber tube filled with an absorbing NIR dye (S109564 Zenecca Limited) and tied into a knot. The inner and outer diameters of the tube were 0.3 and 0.7 mm, respectively, and the absorption coefficient μ_a of the dye was in excess of 10 mm^{-1}. The tube was positioned approximately 3 mm above the detection plane and illuminated in backward mode with the 1064 nm output of the Q-switched Nd:YAG excitation laser as shown in Fig. 11. The excitation laser beam diameter was 22 mm and the fluence 12 mJ/cm^2. The photoacoustic signals were mapped by scanning the sensor interrogation beam over an 11 mm × 11 mm area, in steps of 100 μm. The detected signals were then input to the 3D k-space algorithm [39] referred to in Subsection 2.E in order to reconstruct a 3D image. From this image, maximum intensity projections (MITPs) in the x–y, y–z, and x–z planes were obtained as illustrated in Fig. 12. Comparison with the photograph in Fig. 12 shows that the reconstructed images provide an accurate representation of the target. It is even possible to distinguish the outer wall of the tube from its dye-filled lumen in the close up of the x–y MITP. A range of other absorbing objects, including dye-filled silicone rubber tubes of the same type as above but in different geometrical configurations, were also imaged using the same experimental setup. The lateral (x–y) MITPs of these objects are shown in Fig. 13, again illustrating the ability of the system to provide high-contrast images of absorbing structures. The 3D nature of these images (and that shown in Fig. 12) can be observed in the animated volume rendered images available online.

C. Three-Dimensional Imaging of Blood Vessel Phantom

Although the phantoms used in the previous section are useful for evaluating the ability of the system to obtain 3D images of arbitrarily shaped structures, their relatively high absorption coefficients are not representative of biological tissues—at least not when using excitation wavelengths that provide reasonable penetration depth in tissue. For this reason, a more realistic tissue phantom was constructed. Given the applicability of photoacoustic imaging to visualizing vascular anatomy, this phantom was designed to mimic a network of blood vessels. The phantom, shown in Fig. 14, was composed of a network of randomly orientated PMMA tubes of three inner diameters: 62, 100, and 300 μm. Each tube was filled with human blood of a physiologically realistic hemoglobin concentration (15.2 g/dL). The structure was immersed in an aqueous solution of Intralipid in order to mimic the strong optical scattering of soft tissues. The reduced scattering coefficient of the solution $\mu_s{}'$ was 1 mm^{-1}, which is comparable to that of soft tissues such as those in the breast [42] and skin [43] in the NIR. The setup shown in Fig. 11 was used to image the phantom with the most superficial tube (i.e., that closest to the detection plane) located at z = 0.9 mm and the deepest at z = 5.5 mm. To excite the photoacoustic signals, the output of the OPO, operating at a wavelength of 800 nm was used. The beam diameter was 20 mm and the incident fluence 6.7 mJ/cm^2. As with all the experiments in this study this fluence is well below the MPE for skin. The photoacoustic signals were mapped by scanning the sensor interrogation beam over an area of 14 mm × 14 mm in steps of 100 μm.

Figure 15(b) shows a volume rendered representation (lateral view) of the reconstructed 3D photo-

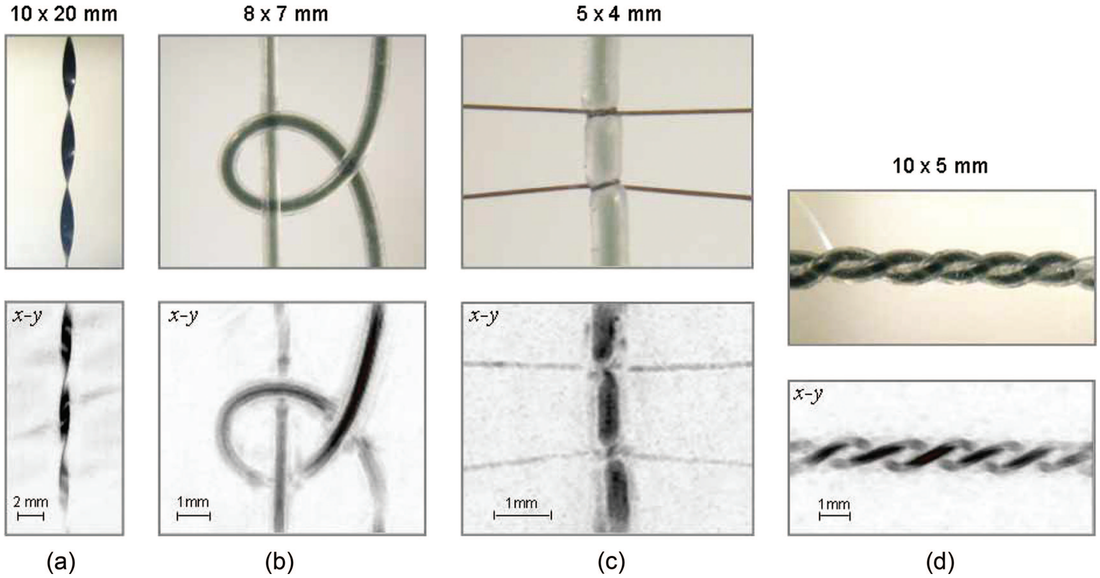

Fig. 13. (Multimedia online; ao.osa.org) (Color online) Photoacoustic images of various absorbing objects obtained using the arrangement shown in Fig. 11. Each object was immersed in Intralipid ($\mu_s{}' = 1\ \text{mm}^{-1}$) and positioned approximately 2 mm above the detection plane. The inner and outer diameter of the tubes was 0.3 and 0.7 mm, respectively. Incident laser fluence $\Phi = 12\ \text{mJ/cm}^2$, $\lambda = 1064$ nm, and pulse duration $t_p = 5.6$ ns. Top row: photographs of objects prior to immersion in Intralipid. Lower row: reconstructed photoacoustic images (x–y MITPs). From left to right: (a) twisted black polymer ribbon. Scan area = 10 mm × 20 mm, dx = 100 μm, dy = 200 μm, and dt = 20 ns. (b) Silicone rubber tubes filled with dye: $\mu_a = 2.7$ (vertical tube) and $\mu_a = 4\ \text{mm}^{-1}$ (looped tube). Scan area = 8 mm × 7 mm, dx = 60 μm, dy = 60 μm, dt = 20 ns. (c) Silicone rubber tube filled with dye ($\mu_a = 2.7\ \text{mm}^{-1}$) and tied with human hair. Scan area = 5 mm × 4 mm, dx = 50 μm, dy = 50 μm, and dt = 8 ns. (d) Twisted pair of silicone rubber tubes filled with dye ($\mu_a = 2.7\ \text{mm}^{-1}$). Scan area = 10 mm × 5 mm, dx = 50 μm, dy = 100 μm, dt = 8 ns.

acoustic image and is clearly in good agreement with the photograph of the same region of the phantom. With the exception of the central 300 μm tube, which was at a distance of $z = 10$ mm from the detection plane, all of the tubes in the photograph are identifiable. An alternative viewing angle of the volume rendered image is shown in Fig. 16, illustrating the 3D nature of the structure. An animated version of this image is also available online.

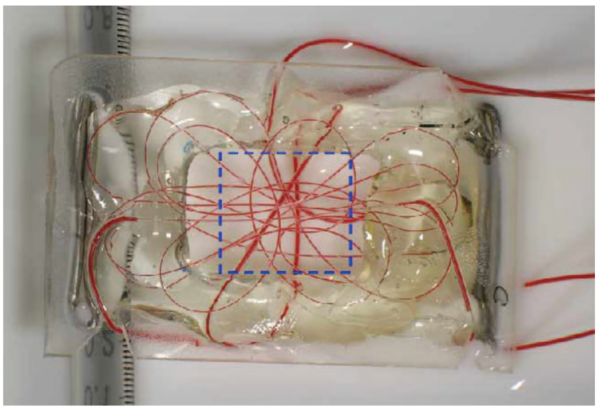

Fig. 14. (Color online) Photograph of blood vessel tissue phantom comprising a network of tubes filled with human blood. The inner diameters of the tubes range from 62 to 300 μm. The white liquid in the background is the Intralipid solution into which the structure was immersed. The dotted line indicates the region of the phantom that was imaged.

D. Multiwavelength Imaging

An important requirement of a photoacoustic imaging instrument is the ability to make measurements at multiple wavelengths in order to spectroscopically identify and quantify the abundance of specific chromophores. These may be endogenous, such as oxyhemoglobin and deoxyhemoglobin, the quantification of which enables blood oxygen saturation [3] to be measured; or they may be exogenous chromophores such as targetted contrast agents used in photoacoustic molecular imaging. To demonstrate the multiwavelength ability of the system, a phantom comprising a row of three tubes made from a fluorinated terpolymer (THV) of nominal inner and outer diameters, 0.8 and 0.94 mm, respectively, was used. Each of the three tubes was filled with one of the following three dyes: ADS645WS, ADS740WS, and ADS830WS (supplied by American Dye Source, Inc.). The absorption spectrum of each dye is shown in Fig. 17. The dyes were mixed with a solution of water and methanol to give a peak absorption coefficient of approximately $0.3\ \text{mm}^{-1}$. The experimental arrangement was similar to that shown in Fig. 7, with the three tubes immersed in Intralipid ($\mu_s{}' = 1\ \text{mm}^{-1}$) and aligned parallel to the y axis at a vertical distance of 4 mm from the detection plane. The sensor interrogation beam was scanned along a line of length 25 mm in steps of 20 μm. Scans were performed at three wavelengths (643, 746, and 822 nm), each chosen to coincide with the absorption peak of one of the dyes. The reconstructed images are shown in Fig. 18 and clearly

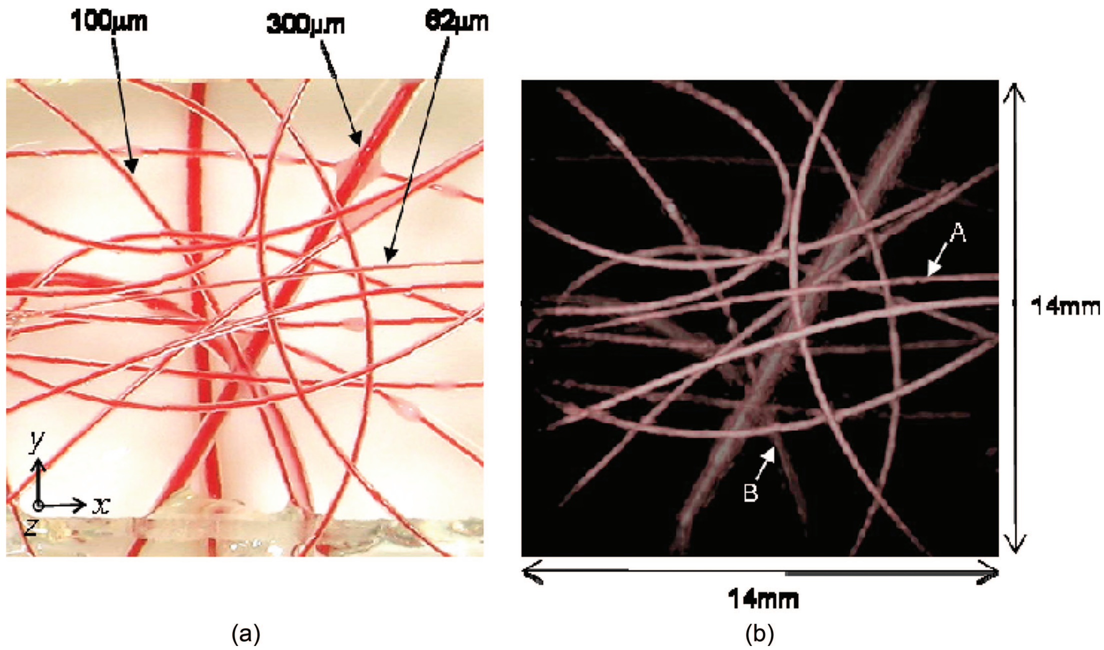

Fig. 15. (Multimedia online; ao.osa.org) (Color online) Photoacoustic image of blood vessel phantom. (a) Photograph showing region of phantom (prior to immersion in Intralipid) that was imaged. (b) Volume rendered 3D photoacoustic image (lateral view). The most superficial tube (A) is located at a vertical distance $z = 0.9$ mm from the detection plane and the deepest (B) was at $z = 5.5$ mm. Scan area $= 14$ mm $\times$ 14 mm, scan step size dx $=$ dy $= 140$ µm, spot diameter $a = 64$ µm, and temporal sampling interval d$t = 20$ ns. Incident laser fluence $\Phi = 6.7$ mJ/cm^2, $\lambda =$ 800 nm, and pulse duration $t_p = 8$ ns.

illustrate the spectral characteristics of the dyes shown in Fig. 17. Thus for the image obtained at 643 nm, the left-hand tube, which is filled with ADS645W and has an absorption coefficient of approximately 0.3 mm^{-1}, is most visible. The center tube, although still visible, displays significantly lower image contrast as it is filled with ADS740WS which, at 643 nm, has an absorption coefficient of approximately 0.04 mm^{-1}. Meanwhile, the right-hand tube, which is filled with ADS830W and has an absorption coefficient of 0.01 mm^{-1}, is barely visible at all. At 746 nm the left-hand tube is no longer visible while the other two tubes can be clearly seen. The center tube displays a contrast that is approximately a factor of 2 higher than the right-hand tube. Finally, at 822 nm the absorption coefficients of ADS645WS and ADS740WS are negligible so only the right-hand tube is visible. Note that the tubes appear correctly in the images as uniformly filled disks, a consequence of the ability of the sensor to measure low frequencies as illustrated in Fig. 6. By contrast the high-pass filtering effect of resonant piezoelectric detectors such as those fabricated from PZT can result in only

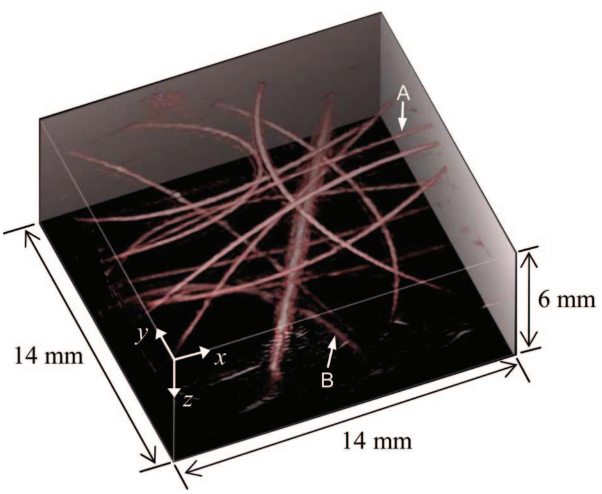

Fig. 16. (Multimedia online; ao.osa.org) (Color online) Alternative viewing angle of volume rendered photoacoustic image shown in Fig. 15(b). Positive z represents the vertical distance from the detection plane. A represents the most superficial tube ($z =$ 0.9 mm) and B the deepest ($z = 5.5$ mm).

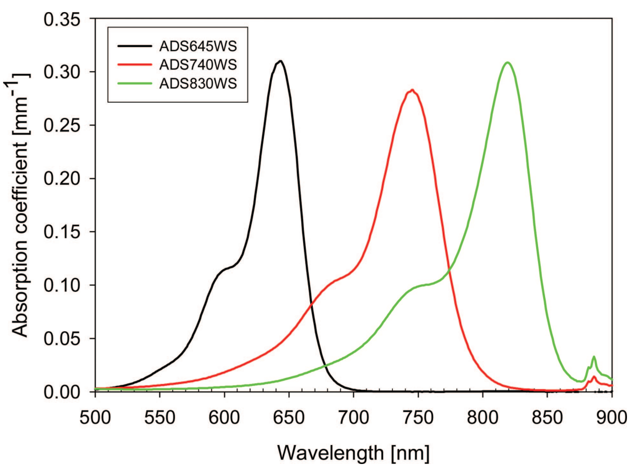

Fig. 17. (Color online) Absorption coefficient spectra of three NIR dyes: ADS645W, ADS740WS, and ADS830WS.

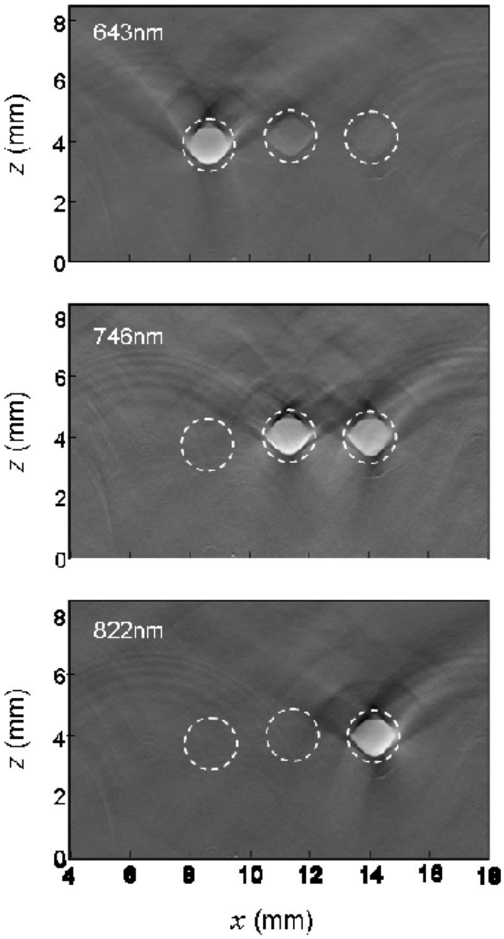

Fig. 18. Two-dimensional photoacoustic images obtained at three wavelengths (643, 746, and 822 nm) of a phantom comprising three tubes filled with different dyes. The absorption spectra of each dye is shown in Fig. 17. The left-hand tube contains ADS645W, the center tube ADS740WS, and the right-hand tube ADS830WS. Line scan length $x = 25$ mm, step size $dx = 20$ μm, and spot size $a = 64$ μm. Temporal sampling interval $dt = 4$ ns. Incident fluence $\Phi = 7$ mJ/cm^2, pulse duration $t_p = 8$ ns.

the edges of relatively large absorbers such as these being observable on the reconstructed image.

4. Conclusions

A new type of high-resolution multiwavelength photoacoustic imaging instrument based upon the use of an optical sensor has been demonstrated. The performance of the system is such that it offers the prospect of providing high-quality 3D images of vascular networks and other absorbing soft tissue structures with a spatial resolution of the order of tens of micrometers with penetration depths of several millimeters. There are several advantages of the concept over existing instruments, particularly those based on piezoelectric detection methods, for high-resolution imaging applications. The transparent nature of the sensor head that enables it to be used in backward mode is the most obvious. The ability to spatially sample the incident acoustic field with higher resolution (approximately tens of micrometers) than can be readily achieved with piezoelectric detectors is also a key distinguishing feature. This along with the uniform wideband frequency response characteristics of the sensor and its high detection sensitivity suggests that the concept may provide a useful alternative to existing instruments for short-range high-resolution photoacoustic imaging.

Although the system in its current form should be able to provide sufficient range and resolution for practical *in vivo* tissue imaging, there remains significant scope to improve its performance. The current instrument can provide a lateral and vertical spatial resolution of approximately 40 and 20 μm, respectively, using the 22 μm FP sensor (-3 dB bandwidth of 39 MHz), an interrogation beam spot diameter of 64 μm, scan step size of 20 μm, and a detection aperture of 40 mm. By reducing the sensor film thickness to 10 μm to increase the bandwidth to 85 MHz and reducing the spot size and step size to 10 μm, it should be possible to achieve a spatial resolution of the order of 10–20 μm. Penetration depth depends essentially on the detector NEP. Currently, the latter is, at best, 0.2 kPa. Ultimately an order of magnitude increase in sensitivity may be possible through a combination of increasing the FPI finesse by increasing the reflectivity of the FPI mirrors and using a higher laser power so that the system becomes shot noise limited. Translating such an increase in sensitivity to a corresponding increase in penetration depth is not entirely deterministic given the myriad of factors involved, but conservatively might be expected to produce a factor of 2 increase enabling penetration depths of up 10 mm in tissue to be achieved.

Acquisition speed is currently impractically slow for most *in vivo* applications at 1 s per scan step. However this is limited by the sequential nature of the waveform downloading process whereby each photoacoustic waveform is downloaded to the PC immediately following its acquisition. By using an acquisition system based upon a segmented memory architecture as described in [33], the complete set of waveforms acquired over the scan can be stored within the on-board memory of the DSO and downloaded to the PC in single step. This would enable acquisition rates limited only by the PRF of the excitation laser to be achieved and provide an order of magnitude decrease in acquisition time to obtain the 3D images presented in this paper. With the advent of higher-repetition-rate lasers [44,45] operating at PRFs as high as several kilohertz there is the opportunity to further reduce acquisition time to the point at which it is limited only by the galvanometer step response time (~0.1 ms). Alternative sensor read-out schemes may allow further reductions in acquisition time. For example, if the detection of the sensor output is accomplished in parallel rather than sequentially using a CCD array of detectors as demonstrated in [46], there is the potential to achieve real-time image acquisition rates.

Given the current and projected performance of the instrument, we can identify the circumstances under which the FP sensor might be used in preference to conventional piezoelectric receivers. Clearly, the transparent nature of the FP sensor head is a feature that most piezoelectric receivers cannot provide and is of critical importance for imaging superficial targets. However for other applications, such as deep tissue imaging or imaging in transmission mode, this feature is not so important. The choice of detector is then determined largely by acoustic performance considerations. When comparing the FP sensor with piezoelectric receivers, the critical issue in this respect is the relationship between detection sensitivity and element size. With piezoelectric receivers, the sensitivity falls off with decreasing element size but with the FP sensor the two are largely independent. As noted in Subsection 2.D.3 this means that once the element size is below a certain threshold then the FP sensor provides higher sensitivity. This threshold depends on a variety of factors such as the NEP of the FP sensor and the material that the piezoelectric receiver is fabricated from. However, given the NEPs reported in this paper and considering piezoelectric PVDF transducers, which, being fabricated from a polymer film have similar broadband frequency response characteristics to the FP sensor and therefore provide a fair comparison, it appears that the threshold lies at a diameter of 1 mm. That is to say a circular PVDF element of smaller diameter will provide a lower sensitivity than the FP sensor. Thus for short range imaging applications (e.g., visualizing the skin microvasculature) where the high-frequency content of the photoacoustic signal (tens of megahertz) demands element sizes on a scale of tens to hundreds of micrometers (this requirement is so that the detector approximates to a pointlike receiver and provides a near omnidirectional response) the FP sensor is likely to be the detector of choice. For longer range applications where penetration depths on a centimeter scale are required (e.g., imaging the breast), the lower frequency content of the signal (<5 MHz) means larger element sizes (millimeter to centimeter dimensions) can be tolerated. For these element dimensions, piezoelectric transducers are more suitable as they will provide higher sensitivity and therefore be better suited to detecting the very weak signals generated at these depths.

One further point to note in relation to the performance of the FP sensor is that, unlike receivers fabricated from piezoceramic materials such as PZT, which tend to be resonant even when heavily damped, the FP sensor provides a truly broadband frequency response down to dc. This ability to measure the-low-frequency content of a photoacoustic signal is important when imaging relatively large or spatially diffuse absorbers. If a resonant detector is used, its high-pass filtering effect can result in only the edges of a large absorbing object appearing on the reconstructed image. If the edges of the object are only weakly defined it may not be visible at all. Apart from the obvious implications of not being able to visualize certain anatomical targets, this can seriously compromise spectroscopic [3] and other techniques [47] that seek to extract quantitative information from the reconstructed image as the latter no longer accurately represents the absorbed optical energy distribution.

In summary, the backward-mode nature of the FP sensor and the high spatial resolution it can provide suggests that it will find a role for high-resolution soft tissue imaging applications. These could include characterizing the structure and function of superficial vascular networks for the assessment of skin tumours, vascular lesions, soft tissue damage such as burns and wounds, and other superficial tissue abnormalities characterized by changes in tissue perfusion.

This work was supported by the UK Engineering and Physical Sciences Research Council (EPSRC).

References

1. M. Xu and L. V. Wang, "Photoacoustic imaging in biomedicine," Rev. Sci. Instrum. **77,** 041101 (2006).
2. J. Laufer, C. E. Elwell, D. T. Delpy, and P. C. Beard, "*In vitro* measurements of absolute blood oxygen saturation using pulsed near-infrared photoacoustic spectroscopy: accuracy and resolution," Phys. Med. Biol. **50,** 4409–4428 (2005).
3. J. G. Laufer, D. T. Delpy, C. E. Elwell, and P. C. Beard, "Quantitative spatially resolved measurement of tissue chromophore concentrations using photoacoustic spectroscopy: application to the measurement of blood oxygenation and haemoglobin concentration," Phys. Med. Biol. **52,** 141–168 (2007).
4. A. A. Oraevsky, E. V. Savateeva, S. V. Solomatin, A. Karabutov, V. G. Andreev, Z. Gatalica, T. Khamapirad, and P. M. Henrichs, "Optoacoustic imaging of blood for visualization and diagnostics of breast cancer," Proc. SPIE **4618,** 81–94 (2002).
5. S. Manohar, A. Kharine, J. C. G. van Hespen, W. Steenbergen, and T. G. van Leeuwen, "The Twente photoacoustic mammoscope: system overview and performance," Phys. Med. Biol. **50,** 2543–2557 (2005).
6. H. F. Zhang, K. Maslov, G. Stoica, and L. V. Wang, "Functional photoacoustic microscopy for high-resolution and noninvasive *in vivo* imaging," Nat. Biotechnol. **24,** 848–850 (2006).
7. J. T. Oh, M. L. Li, H. F. Zhang, K. Maslov, G. Stoica, and L. V. Wang, "Three-dimensional imaging of skin melanoma *in vivo* by dual-wavelength photoacoustic microscopy," J. Biomed. Opt. **11,** 034032 (2006).
8. J. A. Viator, G. Au, G. Paltauf, S. L. Jacques, S. A. Prahl, H. Ren, Z. Chen, and J. S. Nelson, "Clinical testing of a photoacoustic probe for port wine stain depth determination," Lasers Surg. Med. **30,** 141–148 (2002).
9. H. F. Zhang, K. Maslov, G. Soica, and L. V. Wang, "Imaging accute thermal burns by photoacoustic microscopy," J. Biomed. Opt. **11,** 054033 (2006).
10. X. Wang, Y. Pang, G. Ku, X. Xie, G. Stoica, and L. V. Wang, "Noninvasive laser-induced photoacoustic tomography for structural and functional *in vivo* imaging of the brain," Nat. Biotechnol. **21,** 803–806 (2003).
11. E. Z. Zhang, J. Laufer, and P. C. Beard, "Three dimensional photoacoustic imaging of vascular anatomy in small animals using an optical detection system," Proc SPIE **6437,** 643710S (2007).
12. R. A. Kruger, W. L. Kiser, Jr., D. R. Reinecke, G. A. Kruger, and K. D. Miller, "Thermoacoustic optical molecular imaging of small animals," Molecular Imaging **2,** 113–123 (2003).
13. L. Li, R. J. Zemp, L. Gina, G. Stoica, and L. V. Wang, "Photoacoustic imaging of lacZ gene expression *in vivo*," J. Biomed. Opt. **12,** 020504 (2007).
14. X. Xie, M.-L. Li, J.-T. Oh, G. Ku, C. Wang, C. Li, S. Similache, G. F. Lungu, G. Stoica, and L. V. Wang, "Photoacoustic mo-

lecular imaging of small animals *in vivo*," Proc. SPIE **6086** 608606 (2006).

15. X. Wang, Y. Pang, and G. Ku, "Three-dimensional laser-induced photoacoustic tomography of mouse brain with the skin and skull intact," Opt. Lett. **28,** 1739–1741 (2003).
16. R. A. Kruger, K. K. Kopecky, A. M. Aisen, D. R. Reinecke, G. A. Kruger, and W. L. Kiser, "Thermoacoustic CT with radio waves: a medical imaging paradigm," Radiology **211,** 275–278 (1999).
17. J. J. Niederhauser, M. Jaeger, M. Hejazi, H. Keppner, and M. Frenz, "Transparent ITO coated PVDF transducer for opto-acoustic depth profiling," Opt. Commun. **253,** 401–406 (2005).
18. R. G. Kolkmann, E. Hondebrink, W. Steenbergen, and F. F. De Mul, "*In vivo* photoacoustic imaging of blood vessels using an extreme-narrow aperture sensor," IEEE J. Sel. Top. Quantum Electron. **9,** 343–346 (2003).
19. P. Burgholzer, C. Hoffer, G. Paltauf, M. Haltmeier, and O. Scherzer, "Thermoacoustic tomography with integrating and area and line detectors," IEEE Trans. Ultrason. Ferroelectr. Freq. Control **52,** 1577–1583 (2005).
20. K. Koestli, M. Frenz, H. P. Weber, G. Paltauf, and H. Schmidt-Kloiber, "Optoacoustic tomography: time-gated measurement of pressure distributions and image reconstruction," Appl. Opt. **40,** 3800–3809 (2001).
21. B. P. Payne, V. Venugopalan, B. B. Mikc, and N. S. Nishioka, "Optoacoustic tomography using time resolved interferometric detection of surface displacement," J. Biomed. Opt. **8,** 273–280 (2003).
22. J. D. Hamilton and M. O'Donnell, "High frequency ultrasound imaging with optical arrays," IEEE Trans. Ultrason. Ferroelectr. Freq. Control **45,** 216–235 (1998).
23. V. Wilkens and Ch. Koch, "Optical multilayer detection array for fast ultrasonic field mapping," Opt. Lett. **24,** 1026–1028 (1999).
24. P. C. Beard and T. N. Mills, "An optical fibre sensor for the detection of laser generated ultrasound in arterial tissues," Proc. SPIE **2331,** 112–122 (1994).
25. P. C. Beard, F. Perennes, and T. N. Mills, "Transduction mechanisms of the Fabry Perot polymer film sensing concept for wideband ultrasound detection," IEEE Trans. Ultrason. Ferroelectr. Freq. Control **46,** 1575–1582 (1999).
26. Y. Uno and K. Nakamura, "Pressure sensitivity of a fibre-optic microprobe for high frequency ultrasonic field," Jpn. J. Appl. Phys., Part 1 **38,** 3120–3123 (1999).
27. S. Askenazi, R. Witte, and M. O'Donnell, "High frequency ultrasound imaging using a Fabry–Perot etalon," Proc. SPIE **5697,** 243–250 (2005).
28. P. C. Beard, A. Hurrell, and T. N. Mills, "Characterisation of a polymer film optical fibre hydrophone for the measurement of ultrasound fields for use in the range 1–30 MHz: a comparison with PVDF needle and membrane hydrophones," IEEE Trans. Ultrason. Ferroelectr. Freq. Control **47,** 256–264 (2000).
29. E. Z. Zhang, B. T. Cox, and P. C. Beard, "Ultra high sensitivity, wideband Fabry Perot ultrasound sensors as an alternative to piezoelectric PVDF transducers for biomedical photoacoustic detection," Proc. SPIE **5320,** 222–229 (2004).
30. P. C. Beard, E. Z. Zhang, and B. T. Cox, "Transparent Fabry–Perot polymer film ultrasound array for backward-mode photoacoustic imaging," Proc. SPIE **5320,** 230–237 (2004).
31. P. C. Beard, "2D ultrasound receive array using an angle-tuned Fabry Perot polymer film sensor for transducer field characterisation and transmission ultrasound imaging," IEEE Trans. Ultrason. Ferroelectr. Freq. Control **52,** 1002–1012 (2005).
32. P. C. Beard, "Photoacoustic imaging of blood vessel equivalent phantoms," Proc. SPIE **4618,** 54–62 (2002).
33. E. Zhang and P. C. Beard, "Broadband ultrasound field mapping system using a wavelength tuned, optically scanned focussed beam to interrogate a Fabry Perot polymer film sensor," IEEE Trans. Ultrason. Ferroelectr. Freq. Control **53,** 1330–1338 (2006).
34. E. Z. Zhang and P. C. Beard, "2D backward-mode photoacoustic imaging system for NIR (650–1200 nm) spectroscopic biomedical applications," Proc. SPIE **6086,** 60860H (2006).
35. E. Z. Zhang, J. Laufer, and P. C. Beard, "Three dimensional photoacoustic imaging of vascular anatomy in small animals using an optical detection system," Proc. SPIE **6437,** 643710S (2007).
36. H. Yasuda, *Plasma Polymerisation* (Academic, 1985).
37. V. Kozhushko, T. Kholkhlova, A. Zharinov, I. Pelivanov, V. Solomatin, and A. Karabutov, "Focused array transducer for two dimensional optoacoustic tomography," J. Acoust. Soc. Am. **116,** 1498–1506 (2004).
38. B. T. Cox and P. C. Beard, "Frequency dependent directivity of a planar Fabry Perot polymer film ultrasound sensor," IEEE Trans. Ultrason. Ferroelectr. Freq. Control **54,** 394–404 (2007).
39. K. Koestli, M. Frenz, H. Bebie, and H. Weber, "Temporal backward projection of optoacoustic pressure transients using Fourier transform methods," Phys. Med. Biol. **46,** 1863–1872 (2001).
40. K. P. Köstli and P. C. Beard, "Two-dimensional photoacoustic imaging by use of Fourier-transform image reconstruction and a detector with an anisotropic response," Appl. Opt. **42,** 1899–1908 (2003).
41. British Standard, "Safety of laser products. Equipment classification, requirements and user's guide," BS EN60825-1 (The British Standard Institute, 1994).
42. T. A. Troy, D. L. Page, and E. M. Sevic-Mucraca, "Optical properties of normal and diseased breast tissues: prognosis for optical mammography," J. Biomed Opt. **1,** 342–355 (1996).
43. C. R. Simpson, M. Kohl, M. Essenpreis, and M. Cope, "Near-infrared optical properties of *ex vivo* human skin and subcutaneous tissues measured using the Monte Carlo inversion technique," Phys. Med. Biol. **43,** 2465–2478 (1998).
44. K. Mazlov, H. F. Zhang, and L. V. Wang, "Portable real-time photoacoustic microscopy," Proc. SPIE **6437,** 643727 (2007).
45. T. J. Allen and P. C. Beard, "Pulsed NIR laser diode excitation system for biomedical photoacoustic imaging," Opt. Lett. **31,** 3462–3464 (2006).
46. M. Lamont and P. C. Beard, "2D imaging of ultrasound fields using a CCD array to detect the output of a Fabry Perot polymer film sensor," Electron. Lett. **42,** 187–189 (2006).
47. B. T. Cox, S. R. Arridge, K. P. Kostli, and P. C. Beard, "2D quantitative photoacoustic image reconstruction of absorption distributions in scattering media using a simple recursive method," Appl. Opt. **45,** 1866–1875 (2006).